Fourier-domain holography in photorefractive quantum-well films

Kwan Jeong, Leilei Peng, David D. Nolte, and Michael R. Melloch

Fourier-domain holography (FDH) is investigated as a candidate for holographic optical coherence imaging to produce real-time images of structure inside living tissue and turbid media. The effects of spatial filtering, the background intensity distributions, and the role of background noise in determining dynamic range are evaluated for both FDH and image-domain holography (IDH). The grating washout effect in FDH (edge enhancement) is removed by use of a vibrating diffuser that consequently improves the image quality. By comparing holographic images and background images of FDH and IDH we show that FDH provides a higher dynamic range and a higher image quality than IDH for this specific application of imaging diffuse volumetric objects. © 2004 Optical Society of America

OCIS codes: 090.0090, 070.2590, 170.1650, 190.5970, 290.0290, 030.6140.

1. Introduction to Holographic Optical Coherence Imaging

Imaging with light into living tissue has two principal advantages that make it attractive for biomedical imaging applications: It is nonionizing, producing negligible damage to living cells other than thermal effects, and it has the capability of direct imaging with a spatial resolution limited to the wavelength of light near 1 μm. The challenge of using light to image into living tissue, however, is dealing with the multiple scattering that occurs as a result of cell-structure and refractive-index variations. In the near infrared, absorption is relatively small, but scattering extinction coefficients are in the range 10–20 cm^{-1}, which makes it impossible to image much deeper than ~0.1 mm into tissue with the unaided eye. One method of extracting three-dimensional (3D) structural and functional information from living tissue by using light is coherence-domain imaging.

Coherence-domain imaging discards the strong background of diffuse light by using the property of coherence to produce images directly with the singly or weakly scattered light, sometimes called the ballistic light. One widely deployed technique of this approach is optical coherence tomography (OCT), which utilizes confocal scanning in combination with coherence-domain heterodyne detection to reject scattered light. OCT has been developed with extensive progress since the first report in 1991 of imaging through biological samples.[1] OCT has received much attention, with systems achieving high sensitivity with dynamic ranges up to 130 dB.[2] However, OCT and related imaging techniques are not direct in the sense of directly capturing optical images to video because OCT requires point-by-point interferometric scanning and computed reconstruction to produce 3-dimensional spatial information. This restriction currently affects the achievable frame rate, although nearly real-time tomographic reconstruction has been achieved through the use of rapid-scan delay lines.[3]

It is usual to consider approaches to detecting entire coherent images obscured by an incoherent background without the need to scan. Optical coherence imaging (OCI) is a direct optical imaging approach. It is a variant of OCT and uses a dynamic holographic film as a coherence filter to pass only coherent image-bearing light and reject scattered background. Photorefractive holography is ideally suited to produce real-time full-frame coherent images. This full-frame coherent imaging was demonstrated in a photorefractive crystal by French and co-workers of Imperial College, London.[4] Photorefractive quantum-well (PRQW) devices were found to be best suited for this application, because there is no need for Bragg matching to achieve the readout, and the PRQW device pro-

The authors are with Purdue University, West Lafayette, Indiana 47907. K. Jeong (jeongk@physics.purdue.edu), L. Peng, and D. D. Nolte are with the Department of Physics. M. R. Melloch is with the School of Electrical and Computer Engineering.

Received 6 January 2004; revised manuscript received 6 April 2004; accepted 12 April 2004.

0003-6935/04/193802-10$15.00/0

vides an enhanced rejection of diffuse scattered light owing to its inherent insensitivity to an incoherent background. PRQW devices have been used to image through turbid media to depths up to 13 mean-free path[5,6] and have used low-coherence light.[7,8] Holographic OCI has also produced the first depth-resolved images inside living tissue.[9] However, the current generation of PRQW devices has fabrication-related defects that limit the sensitivity and dynamic range of photorefractive holography because of scattered background. The dynamic range (without any spatial filtering) was reported to be 45 dB for the current generation of PRQW devices and is expected to be better than 90 dB for ideal PRQW devices without defects.[10]

Photorefractive holography for OCI to date has used image-domain holography (IDH) exclusively, in which the interference patterns of a direct image in the presence of a reference beam are recorded in a holographic film. The chief advantage of Fourier-domain holography (FDH) for our application is reduced sensitivity to local imperfections, such as dust, scratches, and pits, of the recording media. A point defect in the recording medium becomes a low-level uniform background during holographic image reconstruction. Furthermore, in IDH the spatial resolution is sensitive to the resolution of the recording medium as well as to other optical components, whereas in FDH the spatial resolution is less sensitive to the recording medium's resolution than in IDH.[11,12]

FDH does have the drawback, however, of large intensity variation of the Fourier transform across the recording medium,[6,13] which results in the loss of either high-frequency or low-frequency components in reconstructed images. To solve this problem, diffusers such as random,[13] deterministic,[14] and pseudorandom[15] diffusers were developed after diffused illumination in holography was used by Leith and Upatnieks[16] to provide immunity to local imperfections of optical elements. Although randomly diffused illumination produces speckle noise, this noise can be removed in the reconstructed image through time averaging by use of a moving diffuser.[17]

For these reasons it is attractive to investigate FDH systems by using a vibrating diffuser as a candidate for OCI. In this paper we present a detailed study of a FDH system that uses a vibrating diffuser and a cw narrowband light source. We begin by comparing FDH with IDH and evaluating the spatial filtering effects that reduce spatial resolution. The types of defect in the PRQW device, their intensity distribution as background in the reconstructed holographic image, and the role of background noise in a dynamic range are explored through comparison of FDH with IDH. We provide a complete experimental exploration to show that FDH with a vibrating diffuser provides better image quality and a higher dynamic range than IDH.

2. Fourier-Domain Holography

Holographic image-formation systems can be operated in two limits: IDH and FDH. Distances from

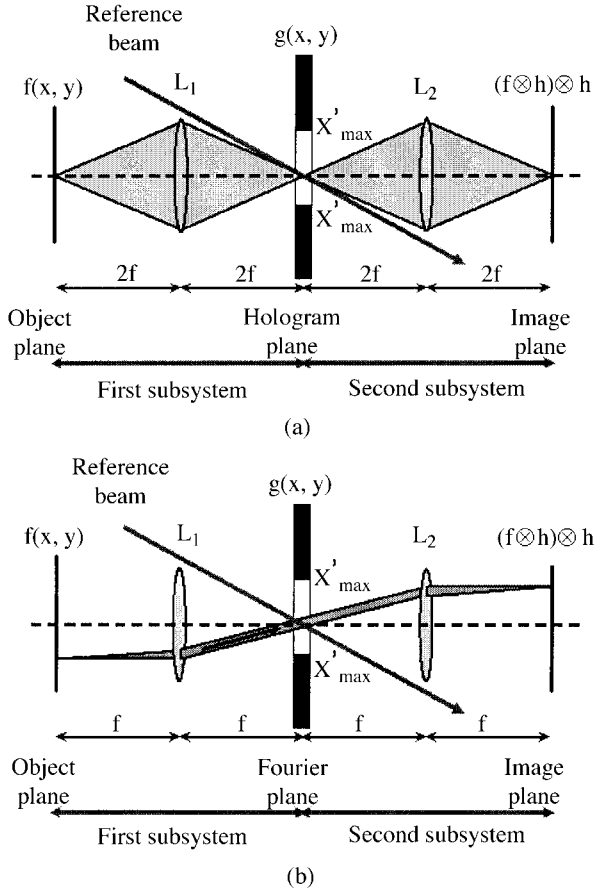

Fig. 1. Schematic figures of (a) IDH and (b) FDH.

each lens to the plane are twice the focal length in IDH, as shown in Fig. 1(a), and a single focal length in FDH, as shown in Fig. 1(b). In IDH, the image formed by the first subsystem is recorded on the recording medium and the holographic image is reimaged by the second subsystem. In FDH, however, the Fourier transform of the object by the first subsystem is recorded on the recording medium and the holographic image is reconstructed by an inverse Fourier transform performed by the second subsystem.

When the wave function at the object plane is $f(x, y)$, the wave function at the recording medium in both IDH and FDH is given by

$$g(x, y) = f(x, y) \otimes h(x, y) = \int_{-\infty}^{\infty}\int_{-\infty}^{\infty} f(x', y')h(x - x', y - y')dx'dy', \quad (1)$$

where $h(x, y)$ is the impulse-response function of the first subsystem. The impulse-response function for IDH is given in the Fresnel approximation by

$$h(x, y) = \frac{\pi D^2}{(4f\lambda)^2}\,\frac{2J_1(\pi D\rho/2f\lambda)}{\pi D\rho/2f\lambda}, \qquad \rho = (x^2 + y^2)^{1/2}, \quad (2)$$

where D is the diameter of the circular aperture, f is the focal length of the lens, λ is the wavelength, and J_1 is a Bessel function of order 1. The impulse-response function for FDH is given in the Fresnel approximation by

$$h(x, y) = -\frac{1}{(f\lambda)^2}\exp\left(-i\frac{4\pi f}{\lambda}\right) \times \exp\left[-i\frac{\pi(x^2+y^2)}{f\lambda}\right]P_1\left(\frac{x}{f\lambda}, \frac{y}{f\lambda}\right), \quad (3)$$

where P_1 is the Fourier transform of the function $p_1(x, y) = p(x, y)\exp[i\pi(x^2 + y^2)/f\lambda]$ and $p(x, y)$ is the pupil function. Pupil function $p(x, y)$ is unity if $(x^2 + y^2)^{1/2} \le D/2$ and zero otherwise. The wave function at the reconstructed image plane in IDH and FDH is now given by $[f(x, y) \otimes h(x, y)] \otimes h(x, y)$ because the first subsystem is geometrically the same as the second. For an ideal lens in IDH, wave function $g(x, y)$ at the recording medium becomes $f(-x, -y)$ and the wave function at the reconstructed image plane becomes $f(x, y)$. For an ideal lens in FDH, the wave function at the Fourier plane (the hologram plane) is given by

$$g(x, y) = \frac{i}{f\lambda}\exp(-i4\pi f/\lambda)F\left(\frac{x}{\lambda f}, \frac{y}{\lambda f}\right), \quad (4)$$

where F is the Fourier transform of $f(x, y)$. The wave function at the image plane in FDH is $f(-x, -y)$ because the second subsystem performs an inverse Fourier transform of $g(x, y)$.

When the cw reference beam (I_r) illuminates the holographic film, an interference pattern of the signal beam (I_s) with the reference beam in the recording medium is given by

$$I(x, y) = [I_r(x, y) + I_s(x, y)][1 + m(x, y)\cos(\mathbf{K}\cdot\mathbf{r})], \quad (5)$$

where $m(x, y)$ is the external modulation index and $\mathbf{K}$ is the grating vector, given by $\mathbf{K} = (2\pi/\Lambda)\hat{\mathbf{K}}$ and

$$m(x, y) = \frac{2[I_r(x, y)I_s(x, y)]^{1/2}}{I_r(x, y) + I_s(x, y)} = \frac{2\sqrt{\beta(x, y)}}{1 + \beta(x, y)}, \quad (6)$$

where Λ is the interference fringe spacing and the beam ratio is $\beta(x, y) = I_r(x, y)/I_s(x, y)$. The signal beam's intensity is $I_s = |g(x, y)|^2$, where $g(x, y)$ is Eq. (1) for IDH and FDH.

The highest spatial frequency that the IDH and FDH systems can transmit is limited by the optical systems and by the holographic film. We identify four important elements that cause spatial filtering in IDH and FDH: the point-spread function (PSF) of the optical system, the window size of the recording medium, the external modulation index dependence of the recording medium, and the fringe-spacing dependence of the recording medium. The PSF results from diffraction and aberration of the components of the imaging system. The PSF limits the spatial bandwidth, which is the highest spatial frequency that the imaging system can transmit. If only the diffraction by the lens aperture causes the PSF, the PSF of the first subsystem in IDH is given by $h(x, y)$ in Eq. (2). The spatial bandwidth imposed by the PSF for the first subsystem is $\nu_s = D/4\lambda f$ in IDH and $\nu_s = D/2\lambda f$ in FDH for coherent illumination, where D is the diameter of the lens.

The PRQW device that is used as our holographic recording medium has a limited window size. The limited window acts as a low-pass filter in FDH, as would a mask in a 4-f system. The spatial bandwidth is given by $\nu_s = W/2\lambda f$ in FDH, where W is the horizontal width of the PRQW device.

The recorded hologram in IDH and FDH depends on the external modulation index because the PRQW device responds to the spatial derivative of the incident beam. When an incident interfering optical field illuminates the PRQW device, carriers that are produced in the brighter regions drift to the darker regions and shield the applied field in the brighter regions. Consequently, the net electric field is distributed into the same spatial distribution as the incident optical intensity. Net carrier transfer is not formed under uniform illumination, and hence a uniform illumination is not recorded. Therefore the PRQW responds to the spatial derivative of the incident optical intensity rather than to the intensity directly. This property gives the PRQW devices the advantage that one can use them to obtain images of structure inside turbid media because only the coherently backscattered light forms stable fringes with the reference light and is recorded by the medium, whereas the incoherent light forms no stationary fringes and hence is not recorded. The diffraction efficiency increases as the external modulation index approaches 1. The external modulation index increases rapidly from 0 to 1 at beam ratios $\beta = 0$–1 and decreases slowly beyond $\beta = 1$.

The Fourier-transformed image of the object at the Fourier plane in FDH has a large variation in intensity; i.e., low-frequency components have much higher intensity than high-frequency components. When the intensity of the low-frequency components is much higher than that of the reference beam, the low-frequency components are washed out as a result of the small modulation index for these frequency components, and only the high-frequency components participate in recording the hologram, which produces high-pass filtering. We call this low-frequency washout in FDH hole burning. We can decrease the signal beam's power to remove this effect, but doing so will result in weak reconstructed holographic images.

The process of dynamic holography in the PRQW device converts external modulation into diffraction gratings that diffract light. The external modulation is converted into an internal modulation of the complex refractive-index gratings through the qua-

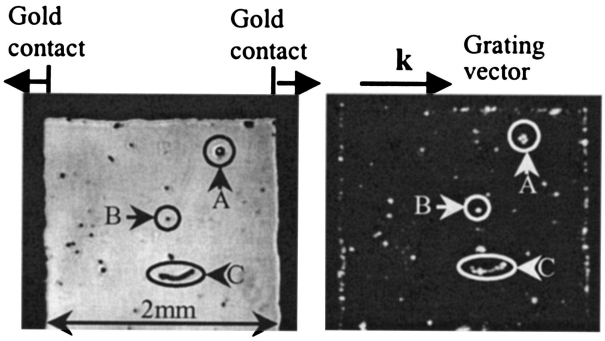

Fig. 2. Direct image of PRQW device BH45, showing several types of defect (labeled A–C) and the corresponding background caused by scattering of the reference beam in the direction of the reconstruction optics and camera.

dratic Franz–Keldysh effect. The internal modulation is given by

$$m_i(\Lambda) = 2m\xi\left[\frac{\Lambda^2}{\Lambda_c{}^2+\Lambda^2}\right], \tag{7}$$

where m is the external modulation index, ξ is the external-to-internal modulation efficiency, Λ is the fringe spacing, and Λ_c is the cutoff fringe spacing.[18] The typical cutoff fringe spacing Λ_c for the current PRQW device is ~ 3 μm, and much smaller cutoff frequencies are possible when a low-temperature-growth PRQW device is used.[19] A fringe spacing that is less than the cutoff fringe spacing is washed out in the process of dynamic holography.

Image quality in coherence imaging is normally degraded by laser speckle, although low-coherence light or a laser with a diffuser may be used to improve image quality. Speckle may be reduced by control of the temporal or spatial coherence of the illuminating beam. Speckle reduction by control of the spatial coherence can be achieved by time averaging of images with a moving diffuser. In such systems the image is stationary in space, and the speckle noise is reduced by time averaging through the motion of the diffuser. The time-averaged images are the same as those obtained in an equivalent incoherent imaging system.[17] Speckle reduction by time-averaging techniques can be achieved in holography. For instance, it has been demonstrated that speckle noise can be reduced in an image averaged during the integration time of a CCD camera by use of a rotating diffuser.[7]

3. Background Scatter and Dynamic Range in Holography

When there are defects inside or on the surface of the recording medium, these defects degrade the holographic image in IDH. Defects in the PRQW device are detected through the direct image, as shown in Fig. 2(a). Figure 2(b) shows the scattered background viewed in the reconstructed image plane in IDH, in which the structure of the scattered light corresponds to the defects in Fig. 2(a). Defects in the PRQW device can be induced during the growth process, in the fabrication process, or simply by use of the device. Examples are shown in circles A and B and in oval C in Fig. 2. Defects during growth are induced inside the structure of the device as structural defects of the multiple quantum well (MQW). Defects in fabrication are induced on the surface of the PRQW device as air bubbles (A and B) or as dust embedded in epoxy. Defects caused by using the device can be created by dust or scratches such as the defect in oval C (Fig. 2). For our PRQW device the defect size in the growth process is less than 1 μm. Defects from fabrication vary from 10 to 100 μm, and the size of the defect in oval C is ~300 μm. In Fig. 2(a) the total area occupied by detectable defects is 0.107 mm^2, the total area of the device is 3.7 mm^2, and total number of detectable defects is 75. The ratio of the area with defects to the total area of the device is 2.9%. The defect density, which is defined as the number of defects per unit area, is ~2000/cm^2. The background shown in Fig. 2(b) results from the scattering of the incident beam from the defects in the PRQW device. The intensity of the scattered beam is given by $I_{\text{scat}} = \eta_{\text{scat}} I_0$, where η_{scat} is the scattering efficiency and I_0 is the incident intensity.

When the hologram is written by signal intensity I_s and reference intensity I_r, the intensity of the diffracted signal, I_d, in a degenerate four-wave mixing configuration is given by

$$I_d = \eta_p m_i{}^2 \frac{I_T{}^2}{(I_T + I_{\text{sat}})^2} I_r, \tag{8}$$

where η_p is the input maximum diffraction efficiency (ratio of incident to diffracted intensities) of the PRQW device, m_i is the internal modulation with external modulation $m = 2\sqrt{I_s I_r}/I_T$, I_{sat} is the saturation intensity of the PRQW device, $I_T = I_s + I_r + I_b$ is the total incident intensity, and I_b is an incoherent background intensity that arises from random scattering of the signal beam in the target. The values of I_{sat} have been experimentally determined to be as small as ~10 μW/cm^2 for an applied field of 5 kV/cm.[20] The diffraction efficiency of our PRQW device was 10^{-3} for an applied field of 5 kV/cm and a fringe spacing of 15 μm but can be as high as 5×10^{-3} under optimal conditions.

The CCD camera is used to observe the holographic images reconstructed from the diffracted beam. The angular separation between the signal and the reference beams is 8° in our experimental configuration. The intensities that reach the CCD are the diffracted beam, the scattered light from the defects in the PRQW, and the tail of the transmitted reference beam through the PRQW. The beam intensity that reaches the CCD camera is then $I_{\text{CCD}} = I_d + I_{\text{scat}} + I_{\text{tr}}$, where I_{tr} is the transmitted reference beam. If the PRQW is illuminated such that $I_T \gg I_{\text{sat}}$, the intensity of the beam on the CCD is given by

$$I_{\text{CCD}} = \eta_p m_i^2 I_r + \eta_{\text{scat}} I_T + I_{\text{tr}}. \tag{9}$$

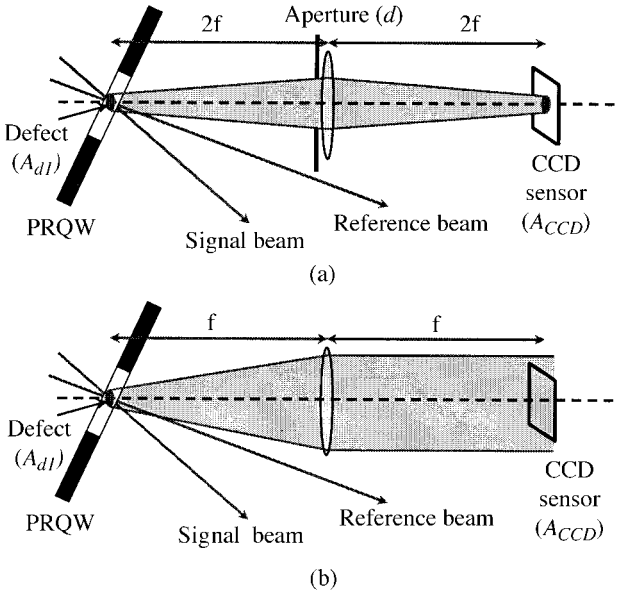

Fig. 3. Schematic figures of the background formation at the CCD camera by the beam scattered from defects in the PRQW film in (a) IDH and (b) FDH. Strong scattering from a localized defect at the film produces a broad low-intensity background in FDH.

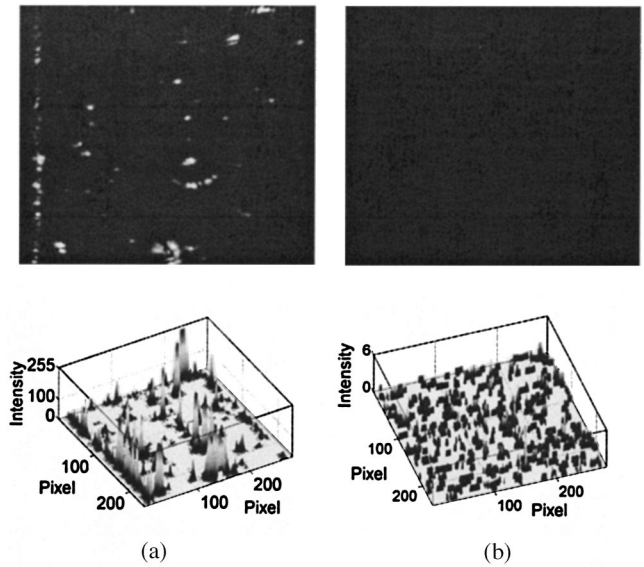

Fig. 4. Scattered background images and the corresponding 3D plots of intensity for a beam ratio $\beta = 0.2$: (a) IDH with a scale of 255 digital numbers and (b) FDH with a scale of 6 digital numbers for the same device.

It has been demonstrated that dynamic range $k_{\max}$ in PRQW holography, which is defined as the maximum detectable ratio of incoherent background to coherent signal, is proportional to the ratio $\eta_p/\eta_{\text{scat}}$ for the nonideal PRQW device.[10] The dynamic range will therefore be increased when η_p increases or η_{scat} decreases.

When the light scattered from defects in the PRQW reaches the CCD camera, the CCD camera is positioned at the image plane of the defects in the PRQW device in IDH and at the Fourier plane in FDH. If there is only one defect with an area A_{d1} in the PRQW, the background image at the CCD camera caused by the beam scattered from a defect will be a replica of this defect in IDH, as shown in Fig. 3(a). However, the background in FDH will be uniformly distributed at the CCD camera, as shown in Fig. 3(b). When the intensity of the scattered beam in IDH at the CCD camera is $I_{\text{scat}}^{\text{IDH}} = \eta_{\text{scat}}^{\text{IDH}} I_T$ and an aperture with a diameter d is used in front of the lens, the intensity of the scattered beam at the lens in IDH is $4A_{d1}\eta_{\text{scat}}^{\text{IDH}} I_{\text{T}} / \pi d^2$ because the total power at the CCD camera is $A_{d1}\eta_{\text{scat}}^{\text{IDH}} I_T$. The intensity of the scattered beam at the lens in FDH is four times that in IDH because the distance from the PRQW to the lens in IDH is twice that in FDH. The intensity of the scattered beam at the CCD camera in FDH is then $I_{\text{scat}}^{\text{FDH}} = 16A_{d1}\eta_{\text{scat}}^{\text{IDH}} I_T / \pi d^2$ because $I_{\text{scat}}^{\text{FDH}}$ at the CCD camera is the same as $I_{\text{scat}}^{\text{FDH}}$ at lens. The ratio of $I_{\text{scat}}^{\text{IDH}} / I_{\text{scat}}^{\text{FDH}}$ is then $\pi d^2/16A_{d1}$. If the total area of defects is A_d, the ratio of the average intensity of the scattered beam at the CCD camera in IDH to that for FDH is given by

$$I_{\text{scat}}^{\text{IDH}}/I_{\text{scat}}^{\text{FDH}} = \eta_{\text{scat}}^{\text{IDH}}/\eta_{\text{scat}}^{\text{FDH}} = \pi d^2/16A_d\,. \qquad (10)$$

The ratio of a dynamic range in FDH to that in IDH is then given by

$$k_{\max}^{\text{FDH}}/k_{\max}^{\text{IDH}} = \pi d^2/16A_d\,. \qquad (11)$$

For typical values of d and A_d, the improvement is ~200, with an enhanced dynamic range of 45 dB for FDH compared with IDH. In addition to the extended dynamic range, FDH exhibits image quality that is dramatically improved because the point defects are removed from the reconstructed image.

Figure 4 shows the difference in the background images for IDH and FDH. Figures 4(a) and 4(b) are the scattered background images and the corresponding 3D plots of intensity with a scale of 255 in IDH and a scale of 6 in FDH, respectively, for beam ratio $\beta = 0.2$. It is clear that in IDH the background image shows replicas of the defects in the PRQW, and the defect images have a high intensity that saturates the CCD. The background image in FDH, however, consists of low-intensity speckle, which is caused by the interference among the scattered beams and has low and uniformly distributed intensity.

4. Results of Experimental Holography

The PRQW devices were used in a transverse-field geometry called the Franz–Keldysh geometry, in which the electric field is applied parallel to the quantum wells. The transverse-field PRQW devices have nonlinear optical properties that have advantages compared with other photorefractive devices, namely, high sensitivity and high-speed response owing to the large absorbance and high carrier mobility of semiconductor materials.[21] The response times of these devices can be adjusted to be faster than standard video rate (30 frames/s), which makes it possi-

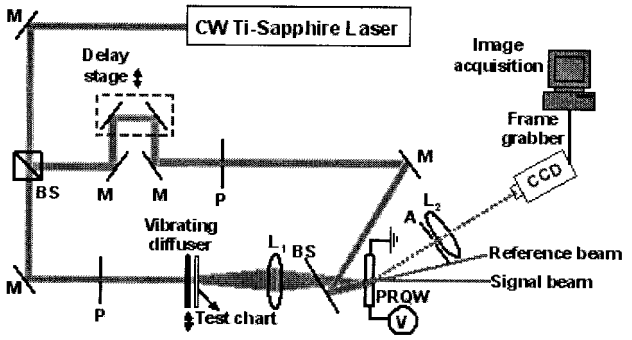

Fig. 5. Experimental setup used to record and reconstruct holograms by use of a vibrating diffuser inserted in front of the USAF test chart: BS, beam splitter; M, mirrors; L_1, L_2, lenses; A, zero-order aperture; P, pinhole; V, voltage.

ble for holographic images of a moving object to be directly displayed in real time on a video monitor.

The MQW structure in the PRQW devices is composed of 100 periods of 7-nm GaAs wells and 6-nm $Al_{0.3}Ga_{0.7}As$ barriers, with a total thickness of 1.3 μm. During growth the MQW layer is sandwiched between 200-nm $Al_{0.2}Ga_{0.8}As$ and 250-nm $Al_{0.2}Ga_{0.8}As$ buffer layers and between 5-nm GaAs and 10-nm GaAs caps to prevent oxidation. The sandwiched MQW was deposited in a series of 10-nm GaAs, 20-nm AlAs, 500-nm $Al_{0.5}Ga_{0.5}As$, and 500-nm GaAs layers, which were deposited on an n + GaAs substrate that was removed by direct etching of the substrate. For the transmission-geometry PRQW the structure was proton implanted to make the device semi-insulating with a double dose of protons $10^{12}/cm^2$ at 160 keV and $5 \times 10^{11}/cm^2$ at 80 keV to introduce deep defects that provide traps for photorefractive space-charge gratings. The structure was then epoxied to a glass substrate, and the semiconductor substrate was removed. We evaporated two gold contacts on to the top of the sample to apply a transverse electric field parallel to the quantum-well layers. Two PRQW devices were used to record and reconstruct holographic images. PRQW device PLO2 has a 1-mm by 2-mm window, and device BH45 has a 2-mm by 2-mm window. All images shown in this paper were acquired with the BH45 device; the PLO2 device was used only to acquire the modulation transfer function (MTF) that is described below.

We used the experimental setup shown in Fig. 5 to record and reconstruct image-domain and Fourier-domain holograms in the PRQW devices, using a tunable cw Ti:sapphire laser pumped by an argon-ion laser and tuned to the PRQW exciton peak (836 nm) to maximize the hologram's diffraction efficiency. The output beam of the cw Ti:sapphire laser passed through a beam splitter to produce a signal and reference beam. The signal beam passed through a U.S. Air Force (USAF) test chart and was relayed by lens L_1 with a focal length of 10 cm onto the PRQW device, where it interfered with the reference beam. The zero path could be adjusted by the delay stage in the reference arm. Fringes from the interference between the signal and reference beam were recorded

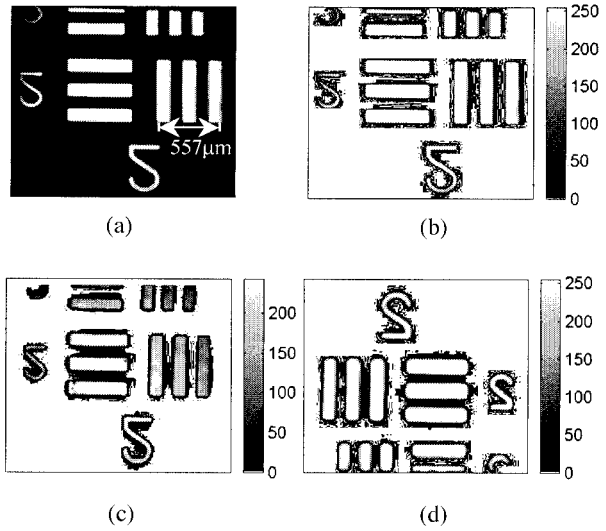

Fig. 6. (a) Direct images of 111-μm-wide bars in a USAF test chart formed by the signal beam without the PRQW device in IDH. (b) Modified direct image of (a) in which zero intensity of the direct image is mapped to white color. Modified direct image transmitted through the PRQW device in (c) an IDH configuration and (d) FDH configuration.

on the PRQW device while a dc field was applied. We reconstructed the hologram by the +1 or −1 diffraction order of the reference beam viewed in a near-IR CCD camera (Hitachi KP-F2A), using lens L_2 with a focal length of 10 cm. The reconstructed holographic images in the CCD camera were captured by a frame grabber in the computer. The distances between the test chart and lens L_1, between lens L_1 and the PRQW device, between the PRQW device and lens L_2, and between L_2 and the CCD camera were 20 cm (twice a focal-length) for IDH and 10 cm (a focal length) for FDH. A diffuser with a diffusing angle of 0.5°, vibrating at a frequency of 42 Hz with an amplitude of 1.6 mm, was introduced in front of the test chart.

The performance of this system was first evaluated for direct images formed by the signal beam. Figure 6(a) shows the direct image of 111-μm-wide bars in a USAF test chart formed by the signal beam without the PRQW device in IDH, and Fig. 6(b) is the modified direct image in which the zero intensity of the direct image is mapped to white color. The effect of the PSF is shown outside the bars in Fig. 6(b). The modified direct images that were transmitted through the PRQW device are shown in Fig. 6(c) for the IDH configuration and in Fig. 6(d) for the FDH configuration. Defects of the PRQW device degrade the image quality of the direct image in IDH through a direct replica of these defects on the direct image, as shown clearly at the left of the third horizontal 111-μm-bar in Fig. 6(c). These defects, however, are not observed in the direct image for FDH because the image plane for the USAF test chart is the Fourier plane for defects of the PRQW device in FDH, and therefore the signal beam diffused by defects forms a relatively uniform background in the Fourier plane.

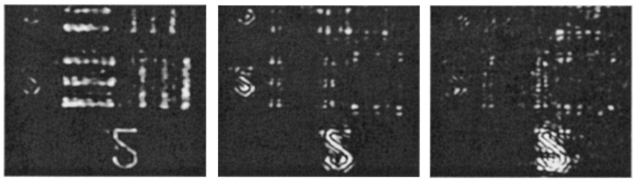

Fig. 7. Holographic reconstructions of a USAF test chart in FDH without a diffuser at fringe spacing $\Lambda = 6$ μm and beam ratios (a) $\beta = 4$, (b) $\beta = 0.2$, and (c) $\beta = 0.01$.

This background is not easily observed in Fig. 6(d) because the intensity of the direct image is much higher than that of the background. The direct image acquired without the PRQW device for FDH has an image quality similar to that of Fig. 6(b), although a comparison of Fig. 6(d) with Fig. 6(b) shows that the image quality in Fig. 6(d) was degraded slightly. The high spatial frequencies of the image were lost by the spatial filtering effect from the 2-mm aperture. In our experimental setup the cutoff frequencies were approximately $1/20\ \mu m^{-1}$ for the direct image without the PRQW device and $1/80\ \mu m^{-1}$ for the direct image with the PRQW device, which were measured from the direct images in FDH.

It has been demonstrated that FDH leads to spatial filtering, which is caused by the large intensity variation in the Fourier plane, and to its associated image degradation.[6] Figure 7 supports this demonstration. Figures 7(a), 7(b), and 7(c) show the holographic reconstructions of a USAF test chart in FDH without a diffuser at a fringe spacing $\Lambda = 6$ μm and beam ratios $\beta = 4$, 0.2, 0.01, respectively. The incident intensity of the reference beam was kept at approximately 20 mW/cm^2, and the electric field applied across the device was +5 kV/cm for all images. The hole-burning effect, which causes high-pass spatial filtering by washing out the low spatial frequencies, is shown in the image at $\beta = 0.2$. The hole-burning effect occurs in FDH because the intensity of the lower spatial frequencies is much higher than that of the higher spatial frequencies and hence the lower spatial frequencies are washed out. Figure 8(a), which shows the Fourier transform of a USAF test chart viewed through the PRQW device in FDH without a diffuser, shows that the center area

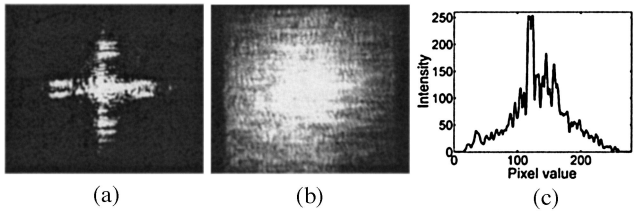

Fig. 8. Images of the optical Fourier transform of a USAF test chart viewed through a PRQW device in FDH (a) without a diffuser and (b) with a vibrating diffuser. (c) Associated intensity line plot at a vertical pixel value of 120 of (b); (b) is the average speckle image during the integration time of the CCD camera.

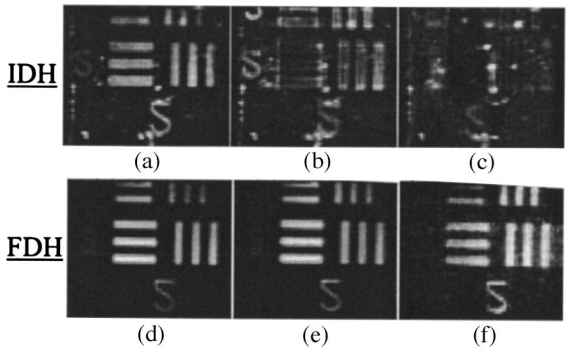

Fig. 9. Holographic reconstructions of a USAF test chart with a vibrating diffuser. Beam ratios are (a) $\beta = 4$, (b) $\beta = 0.2$, (c) $\beta = 0.4$ in IDH and (d) $\beta = 4$, (e) $\beta = 0.2$, (f) $\beta = 0.01$ in FDH; both reconstructions are at a fringe spacing $\Lambda = 6$ μm.

that corresponds to the low spatial frequencies is much brighter than the outer area that corresponds to the high spatial frequencies.

When a vibrating diffuser is introduced in FDH, this hole-burning effect is removed because the large intensity variation in FDH without a diffuser is now altered into the relatively uniform Gaussian distribution of the signal beam on the PRQW device, as shown in Figs. 8(b) and 8(c). The intensity distribution of the signal beam on the PRQW device in IDH is the same as the direct image shown in Fig. 6(a). A comparison of Fig. 8(b) with Fig. 6(a) shows that the intensity in Fig. 8(b) is more uniformly Gaussian distributed on the PRQW device than that in Fig. 6(a). In as much as the incident reference beam has a Gaussian-distributed intensity, the signal beam with a Gaussian-distributed intensity will make the external modulation index at each point on the PRQW device relatively uniform and therefore eliminate the high-pass filter effect. The holographic reconstructions in Fig. 9 show this effect more clearly. Figures 9(a), 9(b), and 9(c) are holographic reconstructions of a USAF test chart in IDH with a vibrating diffuser at beam ratios $\beta = 4$, 0.2, 0.04, respectively, and Figs. 9(d), 9(e), and 9(f) are for FDH with a vibrating diffuser at beam ratios $\beta = 4$, 0.2, 0.01, respectively, at fringe spacing $\Lambda = 6$ μm. At beam ratio $\beta = 0.2$, the holographic image in IDH was spatially filtered because the intensity at the center area of each bar is too high for the hologram to be recorded and is therefore washed out. The effect of spatial filtering was severely enhanced at $\beta = 0.04$, as shown in Fig. 9(c). The hole-burning effect, however, which resulted in spatial filtering in FDH without a diffuser, was completely removed by the Gaussian distribution of the signal beam on the PRQW device through averaged speckles that are formed by a vibrating diffuser, as shown in Figs. 9(d)–9(f).

Figure 10 shows the horizontal MTFs that were examined from the holographic reconstructions of the USAF test chart at beam ratio $\beta = 4$ and at fringe spacing $\Lambda = 15$ μm. The cutoff frequencies that resulted from the static spatial filtering by the limited device window size are $1/167\ \mu m^{-1}$ (6 lines/

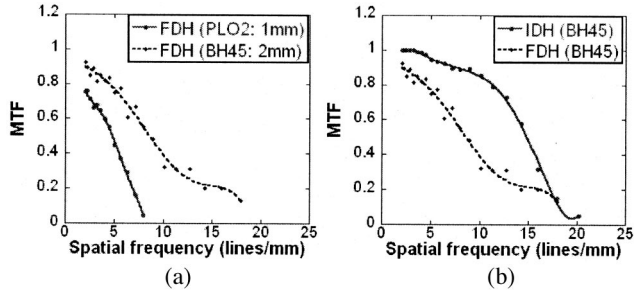

Fig. 10. Horizontal MTFs. (a) FDH for devices with 1-mm window apertures (PLO2) compared with 2-mm window apertures (BH45), showing the effect of Fourier filtering by the smaller window. (b) Comparison of IDH with FDH in a 2-mm device, showing the reduced spatial resolution for FDH with the current setup.

mm) for the 1-mm-width device and 1/83 μm^{-1} (12 lines/mm) for the 2-mm-width device, which were calculated from $v_s = W/2\lambda f$. The difference in the MTF for devices with the 1-mm by 2-mm (PLO2) and 2-mm by 2-mm (BH45) windows in FDH is shown in Fig. 10(a), which corresponds approximately to the calculated values. We also examined the difference between IDH and FDH in the MTF, using the BH45 device, as shown in Fig. 10(b). The cutoff frequency in IDH was calculated from $v_s = D/4\ \lambda f$ to be 1/67 μm^{-1} (15 lines/mm) because the aperture diameter of 5 mm, a focal length of 10 cm, and a wavelength of 840 nm were used for measurement of the MTF. The calculated value closely agrees with the measured values. The MTF is determined by the PSF of the small aperture size in IDH; and the static spatial filtering, by the window size of the PRQW device in FDH.

5. Background Analysis and Dynamic Range

The background intensity in IDH is dependent on the size of the aperture in front of the CCD camera in Fig. 5. The background intensity in FDH, however, as influenced by defects in the PRQW, is hardly changed in correlation with the aperture size. The small diameter of the aperture can be used to make the intensity of scattered background low, but the small size of the aperture decreases the system's resolution. In our IDH configuration the spatial resolution is 33.6 μm for an aperture diameter of 10 mm and a focal length of 10 cm and for a wavelength of 840 nm, calculated from $v_s = D/4\ \lambda f$.

Figures 11(a) and 11(b) show the background image and the corresponding background-subtracted image for the holographic image in Fig. 9(a), and Figs. 11(d) and 11(e) are those for the holographic image in Fig. 9(d). Figures 11(c) and 11(f) show the associated intensity line plots as a function of horizontal pixel value at a vertical pixel number of 108. It is possible to measure the ratio $I_{scat}^{IDH}/I_{scat}^{FDH}$ from the background images. The average of the intensity in IDH, I_{scat}^{IDH}, is 17.0 for Fig. 4(a) and 17.4 for Fig. 11(a) on a scale of 255, which is the sum of all intensities divided by total pixel area. The average intensity in

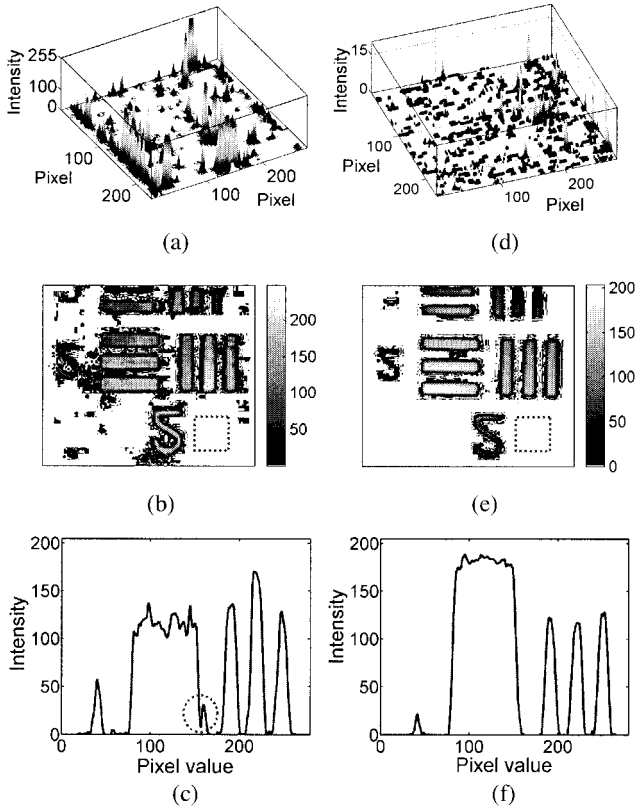

Fig. 11. Background images and the corresponding background-subtracted images in (a) and (b) for IDH and in (d) and (e) for FDH with a vibrating diffuser at beam ratio $\beta = 4$. (c), (f) Associated intensity line plots as a function of horizontal pixel value at a vertical pixel of 108. (b), (e) Images after the corresponding backgrounds are subtracted from Figs. 9 (a) and 9 (d), respectively. The squares in (b) and (e) show the region where the ratio of the dynamic ranges of FDH to IDH is measured, the circle in (c) shows the region where the intensity is abruptly decreased because of a defect.

FDH, I_{scat}^{FDH}, is 0.095 for Fig. 4(b) and 0.120 for Fig. 11(d) on a scale of 255. The measured ratio $I_{scat}^{IDH}/I_{scat}^{FDH}$ is then 180 for Fig. 4 and 145 for Fig. 11. The calculated ratio $I_{scat}^{IDH}/I_{scat}^{FDH}$ was 180 from Eq. (10) for $d = 10$ mm and $A_d = 0.107\ mm^2$. The measured ratios of 180 and 145 closely agree with the calculated ratio of 180. Therefore the dynamic range in a region of background in FDH is 145 times higher than that in IDH in Fig. 11. In IDH the holographic images are reconstructed in the area with little background. To evaluate the ratio of the dynamic ranges of FDH to IDH for such an area with little background we selected the areas marked by rectangles in the images shown in Figs. 11(b) and 11(e). I_{scat}^{IDH} is 1.7 and I_{scat}^{FDH} is 0.13 for this area; hence the measured ratio $I_{scat}^{IDH}/I_{scat}^{FDH}$ becomes 13 for the area with little background. The ratio of dynamic ranges, $k_{max}^{FDH}/k_{max}^{IDH}$, will be increased in proportion to the square of the aperture diameter from Eq. (11) when the aperture with the larger diameter is used for a higher resolution. This ratio also will be increased in inverse proportion to the defect area when the optical quality of

the PRQW device is increased and hence the area of defects is decreased.

The images in Figs. 11(b) and 11(e) show a significant improvement in image quality for FDH relative to IDH, and the curves in Figs. 11(c) and 11(f) show this more clearly. The fluctuation of the intensity in the region of a horizontal bar in Fig. 11(c) results from the high intensity of the background in IDH. The intensity of the horizontal bar in Fig. 11(c) is abruptly decreased to 7 at a pixel value of 158 (see the circled area); this decrease results from a defect at this point. The average intensity of the horizontal bar is 101 with a standard deviation of 34.5 in Fig. 11(c) and is 181 with a standard deviation of 5.82 for Fig. 11(f). As the ratio of a standard deviation to an average intensity becomes lower, the image's homogeneity and fidelity become better. Therefore FDH provides better homogeneity and fidelity of the holographic image than IDH.

If FDH were performed for OCI to detect structure inside a turbid medium, the scattered incoherent light would significantly exceed the image-bearing coherent light, and the reconstructed holographic image would become weak. To evaluate FDH under such conditions we increased the intensity of the incoming signal beam in our FDH configuration. When the signal beam is much higher than the reference beam ($\beta \ll 1$), the intensity of the diffracted signal becomes small [from Eqs. (6) and (8)]. Even though the signal beam at the PRQW device is image-bearing coherent light, the signal beam that reaches the CCD is incoherent light scattered from the defects of the PRQW device. The weak intensity of the reconstructed image and the high intensity of the scattered incoherent light at $\beta \ll 1$ are similar to the conditions for living tissue. Figure 12 shows the background-subtracted holographic images that correspond to the images for FDH in Fig. 9 and the associated intensity line plots at a vertical pixel value of 108. It is clear that FDH with a vibrating diffuser provides a higher image quality than IDH, even when $\beta \ll 1$. This result demonstrates that FDH for OCI can be applicable for detection of structure inside turbid media.

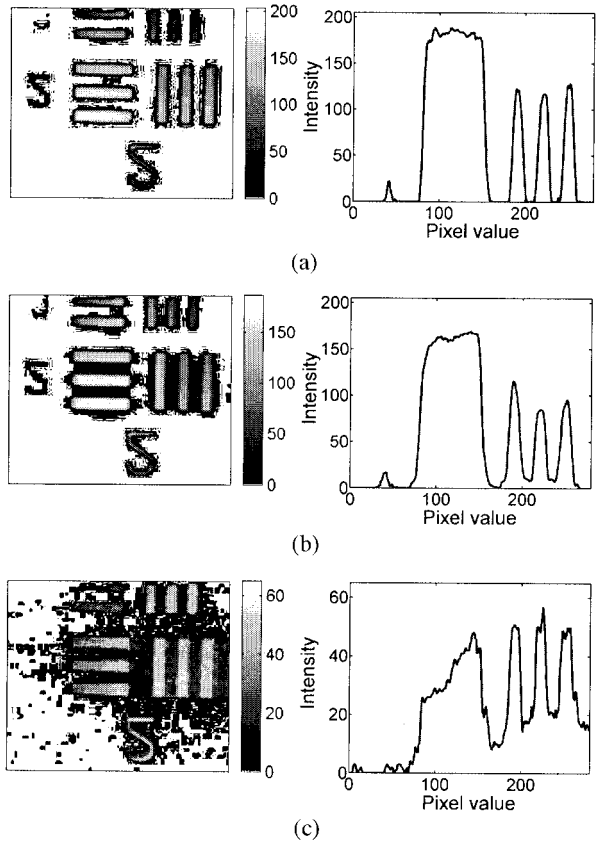

Fig. 12. Background-subtracted holographic images from the FDH results of Fig. 9, showing the associated intensity line plots at a vertical pixel value of 108 at beam ratios $\beta = 4, 0.2, 0.01$ in (a), (b), (c), respectively, with a vibrating diffuser.

6. Discussion

In this paper we have explored fourier-domain holography in photorefractive quantum-well devices for what we believe is the first time as a high-dynamic-range coherent imaging technique. The technique is applicable for imaging through turbid media such as living tissue and is capable of high-speed three-dimensional imaging and real-time acquisition of full-frame holographic images. We have shown that FDH with a vibrating diffuser has the potential to provide significantly better image quality and a higher dynamic range than is possible with image-domain holography. However, FDH has lower resolution than IDH in our current experimental configuration because the window size in the photographic quantum-well device limits the resolution. If a PRQW with a larger window and a lens with smaller focal length are used, the resolution in FDH may be significantly increased. The next step will be the use of the FDH system in a reflection geometry for object imaging and the application of the FDH system to image biological samples, including the use of a mode-locked Ti:sapphire laser to obtain depth-resolved images.

This research was supported by the National Center for Research Resources of the National Institutes of Health under grant R21 RR15040-02 and by the National Science Foundation under grant ECS-0200424.

References

1. D. Huang, E. A. Swanson, C. P. Lin, J. S. Schuman, W. G. Stinson, W. Chang, M. R. Hee, T. Flotte, K. Gregory. C. A. Puliafito, and J. G. Fujimoto, "Optical coherence tomography," Science **254,** 1178–1181 (1991).
2. M. R. Hee, J. A. Izatt, E. A. Swanson, and J. G. Fujimoto, "Femtosecond transillumination tomography in thick tissues," Opt. Lett. **18,** 1107–1109 (1993).
3. A. M. Rollins, M. D. Kulkarni, S. Yazdanfar, R. Ungarunyawee, and J. A. Izatt, "*In vivo* video rate optical coherence tomography," Opt. Express **3,** 219–229 (1998), http://www.opticsexpress.org.
4. S. C. W. Hyde, N. P. Barry, R. Jones, J. C. Dainty, P. M. W. French, M. B. Klein, and B. A. Wechsler, "Depth-resolved ho-

lographic imaging through scattering media by photorefraction," Opt. Lett. **20,** 1331–1333 (1995).
5. R. Jones, S. C. W. Hyde, M. J. Lynn, N. P. Barry, J. C. Dainty, P. M. W. French, K. M. Kwolek, D. D. Nolte, and M. R. Melloch, "Holographic storage and high background imaging using photorefractive multiple quantum wells," Appl. Phys. Lett. **69,** 1837–1839 (1996).
6. R. Jones, N. P. Barry, S. C. W. Hyde, P. M. W. French, K. W. Kwolek, D. D. Nolte, and M. R. Melloch, "Direct-to-video holographic readout in quantum wells for three-dimensional imaging through turbid media," Opt. Lett. **23,** 103–105 (1998).
7. M. Tziraki, R. Jones, P. M. W. French, M. R. Melloch, and D. D. Nolte, "Photorefractive holography for imaging through turbid media using low coherence light," Appl. Phys. B **70,** 151–154 (2000).
8. M. Tziraki, R. Jones, P. French, D. Nolte, and M. Melloch, "Short-coherence photorefractive holography in multiple-quantum-well devices using light-emitting diodes," Appl. Phys. Lett **75,** 363–365 (1999).
9. P. Yu, M. Mustata, J. J. Turek, P. M. W. French, M. R. Melloch, and D. D. Nolte, "Holographic optical coherence imaging of tumor spheroids," Appl. Phys. Lett. **83,** 575–577 (2003).
10. C. Dunsby, Y. Gu, Z. Ansari, P. M. W. French, L. Peng, P. Yu, M. R. Melloch, and D. D. Nolte, "High-speed depth-sectioned wide-field imaging using low-coherence photorefractive holographic microscopy," Opt. Commun. **219,** 87–99 (2003).
11. G. W. Stroke, D. Brumm, and A. Funkhouser, "Three-dimensional holography with 'lensless' Fourier-transform holograms and coarse P/N polaroid film," J. Opt. Soc. Am. **55,** 1327–1328 (1965).
12. W. S. Haddad, D. Cullen, J. C. Solem, J. W. Longworth, A. McPherson, K. Boyer, and C. K. Rhodes, "Fourier-transform holographic microscope," Appl. Opt. **31,** 4973–4978 (1992).
13. C. B. Burckhardt, "Use of random phase mask for the recording of Fourier transform holograms of data masks," Appl. Opt. **9,** 695–700 (1970).
14. W. J. Dallas, "Deterministic diffusers for holography," Appl. Opt. **12,** 1179–1187 (1973).
15. M. Kato, Y. Nakayama, and T. Suzuki, "Speckle reduction in holography with a spatially incoherent source," Appl. Opt. **14,** 1093–1099 (1975).
16. E. N. Leith and J. Upatnieks, "Wavefront reconstruction with diffused illumination and three-dimensional objects," J. Opt. Soc. Am. **54,** 1295–1301 (1964).
17. G. O. Reynolds, J. B. DeVelis, G. B. Parrent, and B. J. Thompson, *Physical Optical Notebook: Tutorials in Fourier Optics* (SPIE, Bellingham, Wash., 1989).
18. D. D. Nolte, S. Balasubramanian, and M. R. Melloch, "Nonlinear charge transport in photorefractive semiconductor quantum wells," Opt. Mater. **18,** 199–203 (2001).
19. D. D. Nolte and M. R. Melloch, "Photorefractive quantum wells and thin films," in *Photorefractive Effects and Materials*, D. D. Nolte, ed. (Kluwer Academic, Dordrecht, The Netherlands, 1995), pp. 373–451.
20. Q. N. Wang, R. M. Brubaker, D. D. Nolte, and M. R. Melloch, "Photorefractive quantum wells: transverse Franz–Keldysh geometry," J. Opt. Soc. Am. B **9,** 1626–1641 (1992).
21. D. D. Nolte, "Semi-insulating semiconductor heterostructures: optoelectronic properties and applications," J. Appl. Phys. **85,** 6259–6289 (1999).